Frontiers of Information Technology & Electronic Engineering
www.jzus.zju.edu.cn; engineering.cae.cn; www.springerlink.com
ISSN 2095-9184 (print); ISSN 2095-9230 (online)
E-mail: jzus@zju.edu.cn

Bidirectional pump controlled reconfigurable nonlinear spoof plasmonic aaveguide*

Wenyi CUI[1], Xinxin GAO[2], Jingjing ZHANG‡[1]

[1]*State Key Laboratory of Millimeter Waves, Southeast University, Nanjing 211189, China*

[2]*State Key Laboratory of Terahertz and Millimeter Waves, City University of Hong Kong, Hong Kong SAR 999077, China*

E-mail: 230228170@seu.edu.cn; xinxigao@cityu.edu.hk; zhangjingjing@seu.edu.cn

Received May 4, 2025; Revision accepted Oct. 2, 2025; Crosschecked

Abstract: We present a dynamically reconfigurable spoof surface plasmon polariton (SSPP) waveguide capable of bidirectional switching between perfect absorption and perfect transmission through active control. Nonlinear varactor diodes are integrated into the waveguide, enabling degenerate phase matching between pump and signal waves via voltage-tuned dispersion engineering. Three-wave mixing processes are established, allowing bidirectional phase-controlled transitions from destructive to constructive interference. The proposed SSPP waveguide overcomes traditional pumping constraints with its bidirectional configuration, supporting both forward- and backward-propagating pump-signal configurations, permitting signal amplitude modulations at both the transmitter and receiver ends. Experimental characterization demonstrates remarkable signal gain tunability: the forward pumping configuration achieves a dynamic range spanning from -69.5 to +1.04 dB, while the backward configuration spans from -70.49 to +1.45 dB. This work provides new design paradigms for microwave coherent systems and advances the development of reconfigurable electromagnetic devices for adaptive energy harvesting and high-speed signal processing applications.

Unedited

Key words: Nonlinear spoof surface plasmon polaritons; Phase-matching; Coherent perfect absorption; Perfect transmission
https://doi.org/10.1631/FITEE.2500286 **CLC number:**

1 Introduction

Absorbers belong to a category of functional devices capable of selectively absorbing electromagnetic energy at specific frequency bands, which can suppress the adjacent-channel or noise interference in communication systems, enhance signal quality and system sensitivity, and convert electromagnetic energy into thermal or electrical energy. These capabilities endow absorbers with significant application value (Chong et al., 2010; Kats & Capasso, 2016; Baranov et al., 2017; Xomalis et al., 2019; Khurgin et al., 2024) in all-optical switches and logic gates (Fang et al., 2014, 2015; Kim et al., 2016; Papaioannou et al., 2016) , photodetectors (Goykhman et al., 2011, 2012, 2016), sensing (Xiao S et al., 2016; Li C et al., 2019; Grimm et al., 2021; Zhang Y et al., 2023), imaging (Monticone et al., 2016; Zhao W et al., 2023), heat transfer control (Li Y et al., 2022), non-destructive measurement (Zanotto et al., 2017), and other fields. Absorption can be achieved through various methods, such as electromagnetic resonance coupling (Li YP et al., 2025; Liao et al., 2015; Wang P et al., 2021), hot electron excitation (Khurgin et al., 2024), and coherent wave interference. Compared to absorbers with fixed parameters, those with dynamically adjustable absorption characteristics (such as absorption rate or operational frequency bands) can significantly enhance the system adaptability and energy efficiency.

‡ Corresponding author

* Project supported by the National Natural Science Foundation of China (Nos. 62271139 and U21A20459), National Key Research and Development Program of China (No. 2022YFA1404903), and the Postgraduate Research & Practice Innovation Program of Jiangsu Province (No. 3304002304D)

ORCID: Wenyi CUI, https://orcid.org/0009-0004-8618-3318; Xinxin GAO, https://orcid.org/0009-0009-3097-6657; Jingjing ZHANG, https://orcid.org/0000-0003-4854-7833

© Zhejiang University Press 2025

For instance, in solar thermal collection systems, adjusting the absorption rates based on light intensity can improve the energy conversion efficiency while preventing overheating. Such devices have become critical components in dynamic electromagnetic regulation systems.

Traditional absorption devices with a tunable absorption rate typically rely on modifying the physical parameters of absorptive materials (e.g., thickness or loss) (Zyablovsky et al., 2014; Pu et al., 2012; Bai et al., 2016; Nie et al., 2014a; Jin and Yu, 2020), or adjusting the phase differences between the counter-propagating coherent waves (Alaee et al., 2020; Chen et al., 2024; Guo and Argyropoulos, 2019, 2020; Huang et al., 2018; Jin and Yu, 2020; Nie et al., 2014a, 2014b; Wan et al., 2011; Wang et al., 2022; Wong et al., 2016; Xiao D et al., 2017; Yan et al., 2014; Zhao H et al., 2016; Zou et al., 2024). However, post-fabrication modification of the physical parameters of the materials is challenging, whereas coherent control over multiple incident waves is simple and can offer enhanced tunability. Notably, low absorption rates do not necessarily correspond to high transmission but may instead indicate high reflection. Conventional high-transmission schemes based on standard interference often induce waveform distortion. To address these limitations, a nonlinear method using degenerate parametric amplification (PA) has been proposed, which enables distortion-free modulation between coherent perfect absorption (CPA) and PA (Cui et al., 2024). However, existing tunable coherent absorption schemes, including the nonlinear PA-CPA approach, face significant constraints: they typically impose strict limitations on the incident direction of the input waves and exhibit constraints in their regulatory dimensions. Although some studies on perfect absorption for multi-angle incident waves have been presented (Luo et al., 2018; Slobodkin et al., 2022), the proposed devices remain incapable of achieving substantial modulation between perfect absorption and perfect transmission. Furthermore, bidirectional perfect absorption-perfect transmission regulation in microwave frequencies using the same device has not yet been reported.

The nonclassical control of wave-field degrees of freedom represents another active research frontier. Techniques such as nonlocal dispersion spectro-polarimetric sampling (Wang X et al., 2024), programmable polarization structuring (S. Wang et al., 2024), and dynamic vectorial holography (Wang ZY et al., 2024) highlight the significant potential of dispersion and phase manipulation for achieving dynamic spectral engineering. Furthermore, spoof surface plasmon polaritons (SSPPs) can effectively mimic the optical surface plasmon polaritons (SPPs) to realize subwavelength field confinements in the microwave regime (Shen et al., 2013), while also enabling dispersion manipulation. Compared with conventional transmission lines like microstrips, SSPP waveguides exhibit superior electromagnetic field localization ability and greater geometric flexibility for functional integration of active components (Zhang HC et al., 2017; Chen ZP et al., 2020). By designing the subwavelength metallic structure and optimizing the parameters of the integrated active elements, SSPP waveguides can achieve unique dispersive properties tailored to meet the demands of different application scenarios.

In recent years, with the development of SSPP manipulation technology, researchers have successfully achieved non-classical dispersion behaviors such as negative dispersion (Zhu et al., 2023; Liu L et al., 2018; Gao et al., 2020; Liu X et al., 2022) and phase matching for multi-wave interference (Liu L et al., 2018; Gao et al., 2020; Liu X et al., 2022; Gao et al., 2021, 2022; Cui and Zhang, 2024). Based on these advancements, second-harmonic generation in forward or backward modes (Gao et al., 2020; Liu L et al., 2018) has been facilitated, and novel functional devices such as nonreciprocal isolators (Gao et al., 2022) and parametric amplifiers (Gao et al., 2021) have been developed. An important advantage of this system is that after sample fabrication, the parameters of the active elements can usually be adjusted by tuning the applied external voltage. This allows for convenient control of the dispersion characteristics without altering the physical structure of the active SSPP waveguides, thus offering reconfigurability.

In this study we exploited the dispersion manipulability of the active SSPP waveguide to satisfy the degenerate phase-matching conditions between pump and signal waves, establishing an interference control mechanism for idler-signal wave interactions during three-wave mixing processes. This approach effectively balances the transmission and reflection of the SSPP waveguide at the pump frequency, innovatively

Unedited

overcoming the traditional limitation requiring unidirectional pump injection relative to the signal. This enables the signal wave to be continuously tuned from a state of perfect absorption to a state of perfect transmission by adjusting the phase of the pump wave, regardless of whether the pump wave is injected co-directionally or counter-directionally with the signal wave. Experimental results revealed that the reflection coefficient S_{11} of the signal wave reaches -30.48 dB (forward pump) and -18.90 dB (backward pump), corresponding to reflected power levels below 1.29%. The output-to-input power ratio exhibits dynamic modulation, ranging from -69.5 to +1.04 dB (forward pump) and from -70.49 to +1.45 dB (backward pump), achieving continuous transition between >98.7% absorption efficiency and 100% transmission. Our scheme enables bidirectional amplitude modulation of signals at both the transmitter and receiver ends, significantly expanding device functionality.

2 Principles to realize nonlinear CPA and perfect transmission

When a high-power pump wave with frequency f_p and a low-power signal wave with frequency f_s simultaneously input into a second-order nonlinear material, three-wave mixing occurs, generating a differential frequency wave (also called as idler wave) with frequency $f_i = f_p - f_s$. When the pump frequency is exactly twice the signal frequency ($f_p = 2f_s$), the generated idler frequency f_{i} equals the signal frequency f_{s}, making the idler wave and the signal wave a pair of coherent waves. Adjust the phase difference between the signal wave and idler wave, and when the coherent waves undergo destructive interference, the signal wave is absorbed, achieving coherent perfect absorption. When the coherent waves undergo constructive interference, the signal wave obtains a gain which can compensate for the loss during transmission in the nonlinear material, achieving perfect transmission. To ensure a constant phase difference between the generated idler and signal waves across different transmission positions, the phase-matching condition must be satisfied. Specifically, the pump wave's phase constant k_p' should be twice the signal wave′s phase constant k_s', and k_s' should equal the idler wave's phase constant k_i'. Under these conditions, the phase mismatch $\Delta k' = k_p' - k_s' - k_i' = 0$ becomes zero, enabling stable interference effects.

By adjusting the phase difference between the input pump wave and signal wave, the phase difference between the generated idler wave and the signal wave can be controlled, thereby regulating the interference behavior between the idler wave and the signal wave. The relationship between the phase difference of the pump-signal pair and that of the signal-idler pair can be derived from the three-wave mixing equations (Cui et al., 2024). The full derivation of this relationship is provided in Supplementary Information Note 1. Let φ_p, φ_s and φ_i denote the initial phases of the pump wave, signal wave and idler wave, respectively. Based on the three-wave mixing equation, we have

$$\varphi_i = 90^\circ - \arg(k_s) + \varphi_p - \varphi_s . \quad (1)$$

By subtracting φ_s from both sides of Eq. (1), the relationship between the phase difference of the signal and idler waves and the phase difference of the input waves is derived as: $\varphi_i - \varphi_s = \varphi_p - 2\varphi_s - \arg(k_s) + 90^\circ = \Delta\varphi + 90^\circ$. Hence, we define the phase difference between the input waves as $\Delta\varphi = \varphi_p - 2\varphi_s - \arg(k_s)$. When $\varphi_i - \varphi_s = 180°$, the signal wave and idler wave are out of phase, and maximum absorption is achieved, corresponding to $\Delta\varphi = 90°$. When $\varphi_i - \varphi_s = 0°$, the signal wave and idler wave are in phase, and maximum gain is achieved, corresponding to $\Delta\varphi = -90°$.

3 Dispersion design of nonlinear SSPP structures

We designed a nonlinear spoof surface plasmon polariton waveguide (Fig. 1) to achieve bidirectional dynamic controls of the signal wave — enabling switching between coherent perfect absorption and perfect transmission by forward or backward pump injection. The nonlinearity of the waveguide is provided by varactor diodes (model: MAVR-011020-1411) soldered on the structure. Fig. 1(a) shows that regardless of whether the pump wave is injected from the input or output port according to the signal wave, the signal wave can be dynamically tuned from perfect absorption to perfect transmission. The waveguide has a period of p=3.3 mm. The detailed unit structure (Fig. 1(b)) has geometric parameters of w=1.15, d=2.8, h=6.85, s=0.3, d_1 =1.5, h_1 =6, x_1=1.9 and x_2=3.3 mm. The front-side metallic tooth

Unedited

is connected to the back-side ground plane through two metallic vias with a radius of 0.2 mm. When designing the structural parameters of the SSPP waveguide, it is important to consider whether its dispersion satisfies phase-matching conditions while balancing the transmission and reflection performance. Taking parameters p and h as examples, in Supplementary Information Note 2 we show how dimensional changes affect the waveguide's dispersion curves and S-parameters.

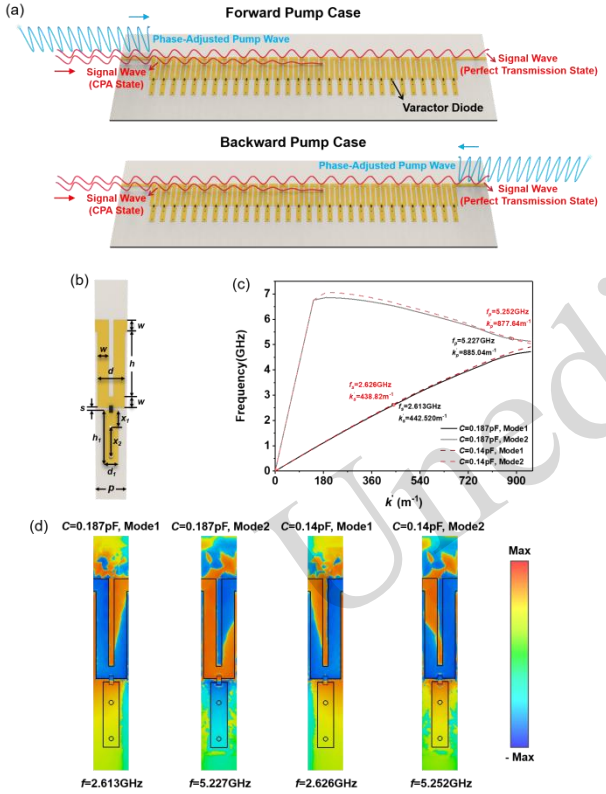

Fig. 1 Nonlinear SSPP waveguide design. (a) Schematic diagram of control based on a nonlinear SSPP waveguide. (b) SSPP unit structure. (c) Simulated dispersion characteristics of the SSPP with varactor diode capacitances *C*=0.187 pF and *C*=0.14 pF, and (d) simulated electric field distributions at four matching points (*f*=2.613 GHz, *f*=5.227 GHz, *f*=2.626 GHz and *f*=5.252 GHz).

Fig. 1(c) shows the lossless dispersion curves of the SSPP unit obtained through eigenmode simulation in the electromagnetic simulation software CST Studio Suite. The results reveal that the designed dispersion curves contain phase-matching points, the positions of which are not sensitive to the varactor diode capacitance C. When C=0.187 pF, the phase-matching condition is satisfied at the signal frequency f_s = 2.613 GHz, and when C=0.14 pF, the phase-matching condition is satisfied at the signal frequency f_s=2.626 GHz. The signal frequency shift is only 0.013 GHz, so the designed structure has a robust immunity to capacitance drift. Furthermore, the pump frequency satisfying the phase-matching condition is intentionally designed at the mode edge for two purposes: to allow the pump wave to simultaneously achieve high reflection and transmission coefficients, and to ensure the pump and signal waves exhibit larger phase constants (k_p', k_s') and shorter wavelengths, thereby enabling a greater number of wavelengths within the same waveguide length. The signal and pump waves with frequencies satisfying $f_p = 2f_s$ and $k_p' = 2k_s'$ are located in the fundamental mode and second-order mode, respectively.

Fig. 1(d) shows the electric field distributions at the signal and pump frequencies satisfying the degenerate phase-matching condition for capacitances C = 0.187 pF and 0.14 pF. The SSPP structure has the advantage of strong field confinement. Fig. 1(d) shows that the electric field is highly localized at the surface of the bending metallic structure and the nonlinear varactor diodes, which facilitates enhanced nonlinear interactions. Furthermore, both the fundamental and second-order modes of the waveguide are hybrid modes combining both even and odd symmetries, exhibiting similar modal field patterns. Crucially, varying the varactor capacitance does not fundamentally alter the inherent modal field patterns; instead, it mainly shifts the resonant frequency of the SSPP unit, thereby modifying the electric field distribution.

4 Simulation and measurement validation

In a practical experiment, we adjusted the applied bias voltage to vary the capacitance of the varactor diode, thereby tuning the dispersion characteristics. Since the dispersion of the designed structure near the matching point is insensitive to the varactor capacitance, the signal wave frequency with optimal control performance (i.e., the highest phase-matching efficiency) consistently remained near 2.6 GHz, while the pump wave frequency was always maintained at twice the signal frequency. Due to errors introduced by different wiring configurations, the optimal bias voltages for co-directional (forward) and counter-directional (backward) inputs of the pump and signal waves differed, measuring 1.29 V and 0.4 V,

Unedited

respectively. The measured matching signal frequency deviated from the simulated one by less than 0.03 GHz, corresponding to an error of about 1.0% of f_s.

Figs. 2(a) and (b) present the simulated and measured S-parameters of a 30-unit SSPP waveguide. As observed, applied bias voltages of 0.4 V and 1.29 V corresponded to varactor diode capacitances of 0.187 pF and 0.14 pF, respectively, and the simulation and measurement results for the S-parameters show excellent agreement. The signal wave exhibited good transmission performance: at bias voltages of 0.4 V and 1.29 V, the S_{21} values were -2.37 dB and -1.96 dB, respectively. Meanwhile, the reflection was low: at bias voltages of 0.4 V and 1.29 V, the S_{11} values were -18.90 dB and -30.48 dB, corresponding to power reflection rates of only 1.29% and 0.09%, respectively. The pump wave maintained a transmission coefficient around -12 dB but showed a reflection coefficient exceeding -5.3 dB, indicating that the pump wave operated in a quasi-resonant mode with both forward-propagating and backward-reflected components.

This ensured that the pump wave, whether co-directionally or counter-directionally input with the signal wave, always contained components sharing the same wave vector direction as the signal wave, satisfying the degenerate phase-matching condition. Figs. 2(c) and (d) show the simulated near-field distributions at the signal and pump wave frequencies for capacitances C=0.187 pF and C=0.14 pF. Dynamic videos of the simulated near-field with phase variation are provided as supplementary materials. The videos show that, at 2.6 GHz, the field exhibited a propagating mode, while at 5.2 GHz, it showed a hybrid mode, in which resonance could be clearly observed in addition to transmission.

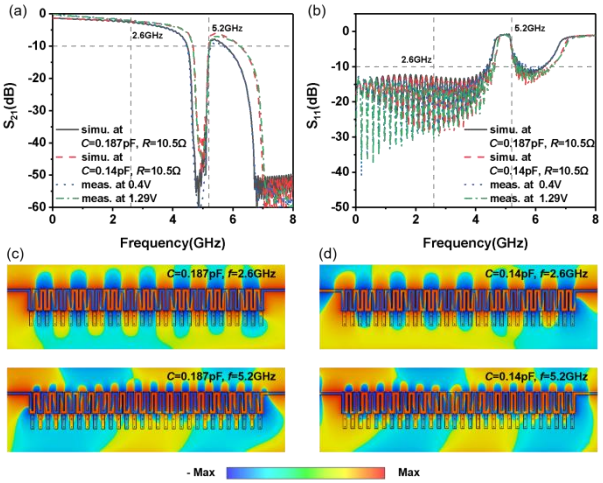

Fig. 2 S-parameters and simulated electric field distributions of the nonlinear SSPP waveguide. (a) Transmission coefficient curves. (b) Reflection coefficient curves. (c) Simulated electric field distributions at the signal and pump frequencies under C=0.187 pF and (d) C=0.14 pF

Based on Zhang LP et al. (2019), we calculated the SSPP dispersion curves under lossy conditions using simulated S-parameter curves that closely matched the measured results. As shown in Fig. 3, for the experimentally measured signal frequency f_s=2.6 GHz and pump wave frequency f_p=2f_s=5.2 GHz, the phase mismatches Δk at varactor diode capacitances C=0.187 pF and C=0.14 pF were calculated as $\Delta k = 907.2 - 443.8 \times 2 = 19.6$ m^{-1} and Δk =911.6−438×2=35.6 m^{-1}, accounting for only 2.16% and 3.91% of k_p', respectively. Therefore, the degenerate phase matching conditions $f_p = 2f_s$ and $k_p' = 2k_s'$ were basically satisfied.

Fig. 4 shows photographs of the nonlinear SSPP waveguide and the experimental setup for dynamic forward/backward control of the signal wave state from perfect transmission to coherent perfect absorption. We used two Agilent E8257D signal generators to generate the signal wave and pump wave, respectively. The signal generator could directly adjust the output phase of the pump wave. An additional power amplifier was connected to enhance the input power of the pump wave due to the limited maximum output power of the signal generator. The circulator exhibited a unidirectional signal flow: Port 1 → Port 2 → Port 3 → Port 1. For forward pumping configuration, both the signal wave and pump wave were coupled through a coupler and input into port 1 of the SSPP

Unedited

waveguide. For backward pumping configuration, the signal wave was directly fed into port 1 of the SSPP waveguide, while the pump wave was introduced into port 2 through a circulator to achieve counter-propagation relative to the signal wave. The pump power coupled into the SSPP waveguide was about 26.9 dBm, whether in the forward-injection or backward-injection configuration. When a signal wave and a pump wave satisfying the degenerate phase matching conditions propagated in the nonlinear SSPP waveguide, the idler wave generated via three-wave mixing, which had the same frequency as the signal wave, interfered with the signal wave, thereby modulating the output power of the signal wave. The output signal wave and pump wave were then received and analyzed by the Agilent N9040B spectrum analyzer. The measured signal wave gain is defined as the ratio of the output power of the signal wave transmitted through the nonlinear SSPP waveguide and modulated by the pump wave to the power of the signal wave directly transmitted to the spectrum analyzer without passing through the nonlinear waveguide.

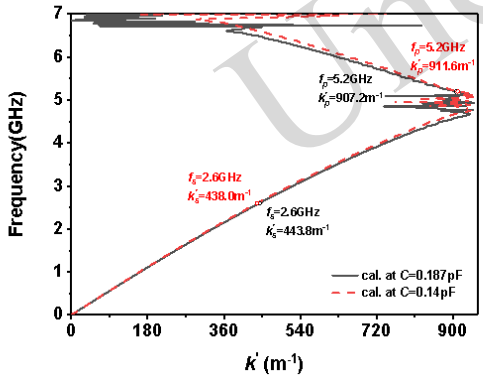

Fig. 3 Calculated dispersion curves of the SSPP waveguide under *C*=0.187 pF and *C*=0.14 pF

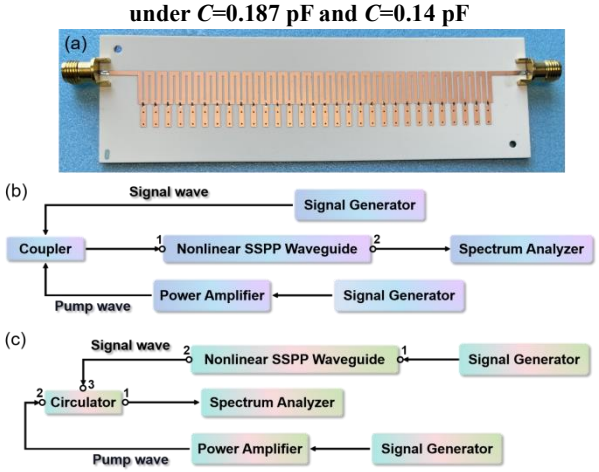

Fig. 4 Photograph of the nonlinear SSPP waveguide and experimental setup for dynamic control of the signal wave from perfect transmission to coherent perfect absorption. (a) Photograph of the SSPP waveguide sample. (b) Experimental setup with forward pump wave incidence. (c) Experimental setup with backward pump wave incidence.

By changing the phase difference $\Delta\varphi = \varphi_p - 2\varphi_s - \arg(k_s)$ between the input pump wave and signal wave, the phase difference between the signal wave and the coherent idler wave can be adjusted, thereby regulating their interference relationship. According to Eq. (1), when $\Delta\varphi = -90°$, the idler wave and the signal wave are in phase, achieving constructive interference and maximizing the output signal power. Conversely, when $\Delta\varphi = 90°$, the idler and signal waves have a $180°$ phase difference, resulting in destructive interference and minimal signal output power. Notably, the idler and signal waves form a coherent pair only when $f_\mathrm{p} = 2f_\mathrm{s}$, and only under this condition can adjusting their phase difference alter the signal power. When $f_\mathrm{p} \neq 2f_\mathrm{s}$, $f_\mathrm{i} \neq f_\mathrm{s}$. Therefore, as shown in Figs. 5(a) and (c), the signal gains at $\Delta\varphi = -90°$ and $90°$ completely overlapped when $f_\mathrm{s} \neq \frac{1}{2}f_\mathrm{p} = 2.6$ GHz, while at the single frequency point $f_\mathrm{s} = 2.6$ GHz, they reached their respective maximum and minimum values. For forward and backward pump wave inputs, the maximum signal gains reached 1.04 dB and 1.45 dB respectively, both exceeding 0 dB to overcome SSPP waveguide losses and achieve perfect transmission. The corresponding minimum gains reached -69.5 dB and -70.49 dB respectively, indicating nearly 100% power attenuation. After subtracting reflected components, both configurations showed an absorption rate of over 98.7%, realizing coherent perfect absorption. Continuous signal gain tuning between its maximum and minimum values can be achieved by varying $\Delta\varphi$ (Figs. 5(b) and (d)). As $\Delta\varphi$ increased from $-90°$ to $90°$, the signal gain decreased slowly initially then dropped rapidly. Extending $\Delta\varphi$ to $270°$ increased the idler-signal phase difference from $180°$ to $360°$, causing the signal gain to symmetrically recover from minimum back to maximum.

Unedited

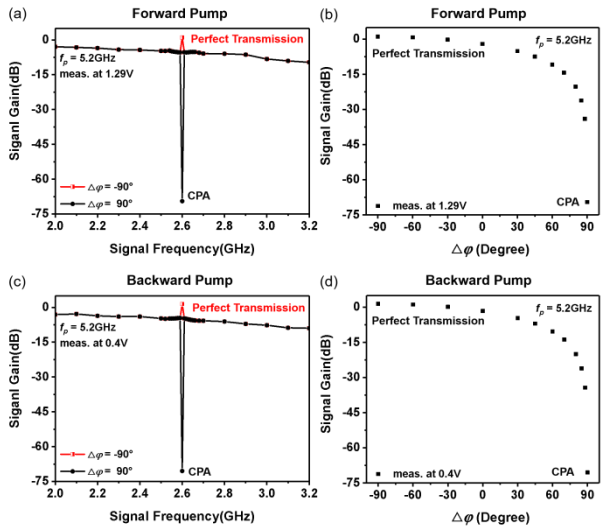

Fig. 5 Signal gain versus signal frequency and input wave phase difference $\Delta\varphi$ with pump frequency $f_p = 5.2$ GHz. (a) Signal gain versus signal frequency under forward pump wave incidence. (b) Signal gain versus input wave phase difference $\Delta\varphi$ under forward pump wave incidence. (c) Signal gain versus signal frequency under backward pump wave incidence. (d) Signal gain versus input wave phase difference $\Delta\varphi$ under backward pump wave incidence

Signal attenuation imposes less stringent requirements on phase-matching accuracy compared to signal amplification. Though loss-compensated perfect transmission is frequency-limited, maintaining $f_p = 2f_s$ through synchronized pump-frequency/voltage tuning enabled over 35 dB attenuation for signals within a 0.5 GHz bandwidth via persistent idler-signal coherence. Details are shown in Supplementary Note 3. In summary, this approach provides continuous transition between an absorption rate of >98.7% and perfect (lossless) transmission. More importantly, as a coherent perfect-absorption device requires phase-matching conditions, it uniquely supports bidirectional pump-wave injection. A functional comparison is given in Supplementary Information Note 4.

5 Conclusions

This paper presents the design of a reconfigurable nonlinear SSPP waveguide capable of dynamically tuning the signal wave from a perfect transmission state to a coherent perfect absorption state, whether the pump wave is injected forward or backward. When the dispersion characteristics of the nonlinear waveguide enable the input signal wave and pump wave to satisfy the degenerate phase matching condition, controlling the phase difference between input waves can modify the phase relationship between the coherent pair of idler and signal waves, thereby continuously adjusting the signal wave gain. Experimental results show that the designed SSPP waveguide achieved a power reflectance below 1.29% at the signal frequency. Regardless of co-directional or contra-directional input of pump and signal waves into the nonlinear waveguide, adjusting the phase difference between input waves enabled the signal wave to attain over 100% transmittance (perfect transmission) and a 98.7% absorption rate (coherent perfect absorption). The demonstrated capability to switch between extreme absorption and transmission states in a single microwave device, regardless of the direction of pump propagation, overcomes conventional limitations in unidirectional coherent control systems.

Unedited

Contributors

Jingjing ZHANG designed the research. Wenyi CUI processed the data. Wenyi CUI drafted the paper. Xinxin GAO and Jingjing ZHANG helped organize the paper. Wenyi CUI and Jingjing ZHANG revised and finalized the paper.

Conflict of interest

All the authors declare that they have no conflict of interest.

References

Alaee R, Vaddi Y, Boyd RW, 2020. Dynamic coherent perfect absorption in nonlinear metasurfaces. *Opt Lett*, 45(23):6414-6417. https://doi.org/10.1364/OL.402380

Bai P, Ding K, Wang G, et al., 2016. Simultaneous realization of a coherent perfect absorber and laser by zero-index media with both gain and loss. *Phys Rev A*, 94(6):063841. https://doi.org/10.1103/PhysRevA.94.063841

Baranov DG, Krasnok A, Shegai T, et al., 2017. Coherent perfect absorbers: linear control of light with light. *Nat Rev Mater*,2(12):17064. https://doi.org/10.1038/natrevmats.2017.64

Chen JT, Hong LJ, Lei JT, et al., 2024. High-performance terahertz coherent perfect absorption with asymmetric. Graphene metasurface. *Photonics*, 11(6):544. https://doi.org/10.3390/photonics11060544

Chen ZP, Lu WB, Liu ZG, et al., 2020. Dynamically tunable integrated device for attenuation, amplification, and transmission of SSPP using graphene. IEEE Trans Antennas Propagat,68(5):3953-3962. https://doi.org/10.1109/TAP.2020.2963946

Chong YD, Ge L, Cao H, et al., 2010. Coherent perfect absorbers: time-reversed lasers. *Phys Rev Lett*, 105(5):053901. https://doi.org/10.1103/PhysRevLett.105.053901

Cui WY, Zhang JJ, 2024. Nonlinear coherent perfect absorption based on second harmonic generation in a spoof plasmonic waveguide. 2024 Cross Strait Radio Science and Wireless Technology Conf (CSRSWTC), p.1-3. https://doi.org/10.1109/CSRSWTC64338.2024.10811616

Cui WY, Zhang JJ, Luo Y, et al., 2024. Dynamic switching from coherent perfect absorption to parametric amplification in a nonlinear spoof plasmonic waveguide. *Nat Commun*, 15(1):2824. https://doi.org/10.1038/s41467-024-47191-x

Fang X, Lun Tseng M, Ou JY, et al., 2014. Ultrafast all-optical switching via coherent modulation of metamaterial absorption.*Appl Phys Lett*, 104(14):141102. https://doi.org/10.1063/1.4870635

Fang X, MacDonald KF, Zheludev NI, 2015. Controlling light with light using coherent metadevices: all-optical transistor, summator and invertor. *Light: Sci Appl*, 4(5):e292-e292. https://doi.org/10.1038/lsa.2015.65

Gao XX, Zhang JJ, Zhang HC, et al., 2020. Dynamic controls of second-harmonic generations in both forward and backward modes using reconfigurable plasmonic metawaveguide. *Adv Opt Mater*, 8(8):1902058. https://doi.org/10.1002/adom.201902058

Gao XX, Zhang JJ, Luo Y, et al., 2021. Reconfigurable parametric amplifications of spoof surface plasmons. *Adv Sci*, 8(17):2100795. https://doi.org/10.1002/advs.202100795

Gao XX, Zhang JJ, Ma Q, et al., 2022. Nonmagnetic spoof plasmonic isolator based on parametric amplification. *Laser Photon Rev*, 16(4):2100578. https://doi.org/10.1002/lpor.202100578

Goykhman I, Desiatov B, Khurgin J, et al., 2011. Locally oxidized silicon surface-plasmon Schottky detector for telecom regime. *Nano Lett*, 11(6):2219-2224. https://doi.org/10.1021/nl200187

Goykhman I, Desiatov B, Khurgin J, et al., 2012. Waveguide based compact silicon Schottky photodetector with enhanced responsivity in the telecom spectral band. *Opt Express*,20(27):28594. https://doi.org/10.1364/OE.20.028594

Goykhman I, Sassi U, Desiatov B, et al., 2016. On-chip integrated, silicon–graphene plasmonic Schottky photodetector with high responsivity and avalanche photogain. *Nano Lett*, 16(5):3005-3013. https://doi.org/10.1021/acs.nanolett.5b05216

Grimm P, Razinskas G, Huang JS, et al., 2021. Driving plasmonic nanoantennas at perfect impedance matching using generalized coherent perfect absorption. *Nanophotonics*, 10(7):1879-1887. https://doi.org/10.1515/nanoph-2021-0048

Guo TJ, Argyropoulos C, 2019. Tunable and broadband coherent perfect absorption by ultrathin black phosphorus metasurfaces. *J Opt Soc Am B*, 36(11):2962-2971. https://doi.org/10.1364/JOSAB.36.002962

Guo TJ, Argyropoulos C, 2020. Nonlinear and amplification response with asymmetric graphene-based coherent perfect absorbers. 2020 IEEE Int Symp on Antennas and Propagation and North American Radio Science Meeting, p.727-728. https://doi.org/10.1109/IEEECONF35879.2020.9330288

Huang S, Xie ZW, Chen WD, et al., 2018. Metasurface with multi-sized structure for multi-band coherent perfect absorption. *OptExpress*, 26(6):7066-7078. https://doi.org/10.1364/OE.26.007066

Jin Y, Yu K, 2020. Broadband single-channel coherent perfect absorption with a perfect magnetic mirror. *Opt Express*, 28(23):35108. https://doi.org/10.1364/OE.408494

Kats MA, Capasso F, 2016. Optical absorbers based on strong interference in ultra-thin films. *Laser Photon Rev*, 10(5):735-749. https://doi.org/10.1002/lpor.201600098

Khurgin J, Bykov AY, Zayats AV, 2024. Hot-electron dynamics in plasmonic nanostructures: fundamentals, applications and overlooked aspects. *eLight*, 4(1):15. https://doi.org/10.1186/s43593-024-00070-w

Kim J, Kwon J, Kim M, et al., 2016. Low-dielectric-constant polyimide aerogel composite films with low water uptake. *Polym J*, 48(7):829-834. https://doi.org/10.1038/pj.2016.37

Li CW, Qiu JL, Ou JY, et al., 2019. High-sensitivity refractive index sensors using coherent perfect absorption on graphene in the vis-NIR region. *ACS Appl Nano Mater*, 2(5):3231-3237. https://doi.org/10.1021/acsanm.9b00523

Li Y, Qi MH, Li JX, et al., 2022. Heat transfer control using a thermal analogue of coherent perfect absorption. *Nat Commun*, 13(1):2683. https://doi.org/10.1038/s41467-022-30023-1

Li YP, Guo ZH, Zhang HF, 2025. Dispersion characteristics-based asymmetric frequency selective rasorber using spoof surface plasmon polariton mode. *Opt Laser Technol*, 181:111718. https://doi.org/10.1016/j.optlastec.2024.111718

Liao Z, Shen XP, Pan BC, et al., 2015. Combined system for efficient excitation and capture of LSP resonances and flexible control of SPP transmissions. *ACS Photon*, 2(6):738-743. https://doi.org/10.1021/acsphotonics.5b00096

Liu LL, Wu L, Zhang JJ, et al., 2018. Backward phase matching for second harmonic generation in negative‐index conformal surface plasmonic metamaterials. *Adv Sci*, 5(11):1800661. https://doi.org/10.1002/advs.201800661

Liu XY, Lei Y, Zheng X, et al., 2022. Reconfigurable spoof plasmonic coupler for dynamic switching between forward and backward propagations. *Adv Mater Technol*, 7(8):2200129. https://doi.org/10.1002/admt.202200129

Luo J, Liu BB, Hang ZH, et al., 2018. Coherent perfect absorption via photonic doping of zero-index media. *Laser Photon Rev*, 12(8):1800001. https://doi.org/10.1002/lpor.201800001

Monticone F, Valagiannopoulos CA, Alù A, 2016. Parity-time

Uncited

symmetric nonlocal metasurfaces: all-angle negative refraction and volumetric imaging. *Phys Rev X*, 6(4):041018. https://doi.org/10.1103/PhysRevX.6.041018

Nie GY, Shi QC, Zhu Z, et al., 2014a. Coherent perfect absorber based on metamaterials. Proc SPIE 9278, Plasmonics, article 92780B. https://doi.org/10.1117/12.2071448

Nie GY, Shi QC, Zhu Z, et al., 2014b. Selective coherent perfect absorption in metamaterials. *Appl Phys Lett*, 105(20):201909. https://doi.org/10.1063/1.4902330

Papaioannou M, Plum E, Valente J, et al., 2016. Invited Article: all-optical multichannel logic based on coherent perfect absorption in a plasmonic metamaterial. *APL Photon*, 1(9):090801. https://doi.org/10.1063/1.4966269

Pu MB, Feng Q, Wang M, et al., 2012. Ultrathin broadband nearly perfect absorber with symmetrical coherent illumination. *Opt Express*, 20(3):2246. https://doi.org/10.1364/OE.20.002246

Shen XP, Cui TJ, Martin-Cano D, et al., 2013. Conformal surface plasmons propagating on ultrathin and flexible films. *Proc Natl Acad Sci USA*, 110(1):40-45. https://doi.org/10.1073/pnas.1210417110

Slobodkin Y, Weinberg G, Hörner H, et al., 2022. Massively degenerate coherent perfect absorber for arbitrary wavefronts. *Science*, 377(6609):995-998. https://doi.org/10.1126/science.abq8103

Wan WJ, Chong YD, Ge L, et al., 2011. Time-reversed lasing and interferometric control of absorption. *Science*, 331(6019):889-892.
https://doi.org/10.1126/science.1200735

Wang C, Shen X, Chu HC, et al., 2022. Realization of broadband coherent perfect absorption of spoof surface plasmon polaritons. *Appl Phys Lett*, 120(17):171703. https://doi.org/10.1063/5.0089065

Wang P, Shen XP, Zhang HC, et al., 2021. Assembly-induced microwave band resonance in gold nanoparticles-based ultrathin and flexible spoof localized surface plasmon. *Mater Design*, 204:109622. https://doi.org/10.1016/j.matdes.2021.109622

Wang SJ, Qin WT, Guan TY, et al., 2024. Flexible generation of structured terahertz fields via programmable exchange-biased spintronic emitters. *eLight*, 4(1):11. https://doi.org/10.1186/s43593-024-00069-3

Wang XJ, Van Mechelen T, Bharadwaj S, et al., 2024. Exploiting universal nonlocal dispersion in optically active materials for spectro-polarimetric computational imaging. *eLight*, 4(1):22. https://doi.org/10.1186/s43593-024-00078-2

Wang ZY, Zhou Z, Zhang H, et al., 2024. Vectorial liquid-crystal holography. *eLight*, 4(1):5. https://doi.org/10.1186/s43593-024-00061-x

Wong ZJ, Xu YL, Kim J, et al., 2016. Lasing and anti-lasing in a single cavity. *Nat Photon*, 10(12):796-801. https://doi.org/10.1038/nphoton.2016.216

Xiao D, Tao KY, Wang Q, et al., 2017. Metasurface for multi-wavelength coherent perfect absorption. *IEEE Photon J*, 9(1):6800108. https://doi.org/10.1109/JPHOT.2016.2636019

Xiao SY, Gear J, Rotter S, et al., 2016. Effective PT-symmetric metasurfaces for subwavelength amplified sensing. *New J Phys*, 18(8):085004. https://doi.org/10.1088/1367-2630/18/8/085004

Xomalis A, Jung Y, Demirtzioglou I, et al., 2019. Nonlinear control of coherent absorption and its optical signal processing applications. *APL Photon*, 4(10):106109. https://doi.org/10.1063/1.5123547

Yan XB, Cui CL, Gu KH, et al., 2014. Coherent perfect absorption, transmission, and synthesis in a double-cavity optomechanical system. *Opt Express*, 22(5):4886-4895. https://doi.org/10.1364/OE.22.004886

Zanotto S, Bianco F, Miseikis V, et al., 2017. Coherent absorption of light by graphene and other optically conducting surfaces in realistic on-substrate configurations. *APL Photon*, 2(1):016101. https://doi.org/10.1063/1.4967802

Zhang HC, Cui TJ, Xu J, et al., 2017. Real-time controls of designer surface plasmon polaritons using programmable plasmonic metamaterial. *Adv Mater Technol*, 2(1):1600202. https://doi.org/10.1002/admt.201600202

Zhang LP, Zhang HC, Gao Z, et al., 2019. Measurement method of dispersion curves for spoof surface plasmon polaritons. *IEEE Trans Antennas Propagat*, 67(7):4920-4923. https://doi.org/10.1109/TAP.2019.2916645

Zhang Y, Zhang D, Zhang HF, 2023. A functionality-switchable device based on coherent perfect absorption with narrowband absorbing performance and sensing function. *Phys Scr*, 98(3):035502. https://doi.org/10.1088/1402-4896/acb672

Zhao H, Fegadolli WS, Yu JK, et al., 2016. Metawaveguide for asymmetric interferometric light-light switching. *Phys Rev Lett*, 117(19):193901. https://doi.org/10.1103/PhysRevLett.117.193901

Zhao WL, Chen M, Wang XY, et al., 2023. Multidimensional tunable graphene chiral metasurface based on coherent control. *Opt Lett*, 48(19):5153. https://doi.org/10.1364/OL.500735

Zhu B, Hu MZ, Xu J, et al., 2023. Plasmonic dual-band waveguide with independently controllable band-notched characteristics. *Appl Phys Express*, 16(8):086001. https://doi.org/10.35848/1882-0786/acedea

Zou W, Guo TJ, Argyropoulos C, 2024. Ultrabroadband coherent perfect absorption with composite graphene metasurfaces. *Opt Express*, 32(19):32667. https://doi.org/10.1364/OE.534828

Zyablovsky AA, Vinogradov AP, Pukhov AA, et al., 2014. PT-symmetry in optics. *Phys Usp*, 57(11):1063-1082. https://doi.org/10.3367/UFNe.0184.201411b.1177

Unedited